joires 7(1), June, 2026.
ISSN: 2141-8217.
https://journals.unizik.edu.ng/ joires/about

Development of Sb_2S_3 as a double absorber layer with Sb_2Se_3 by Simple and Low Cost Chemical Bath Deposition Technique for Solar Cell Applications

(pp. 666-681.)

James Abumchukwu Ezihe, Ph.D
Department of Physics,
School of Physical Sciences,
Federal University of Technology, P.M.B. 1526 Owerri
Nigeria

Correspondence email: james.ezihe@futo.edu.ng

Abstract: Antimony sulfide (Sb_2S_3) has been explored for its potential in optoelectronic applications. It was synthesized using a low-cost and facale chemical bath deposition (CBD) method. The resulting material showed an orange color, consistent with previous reports. This study focused on examining how varying concentrations of sodium thiosulphate ($Na_2S_2O_3$) affect the optical and morphological characteristics of **Sb_2S_3**. Additionally, the impact of annealing on these properties was also analyzed. Comprehensive characterization was carried out to assess structural, optical, and surface features. X-ray diffraction (XRD) results indicated that the as-deposited **Sb_2S_3** films were amorphous. However, annealing at 200 °C enhanced the crystallinity of the material. Optically, the film deposited with a 2.0 M concentration showed 99% absorption in the blue line (450–495 nm) of the visible spectrum, while the 2.5 M sample exhibited similar absorption in the UV range. An increase in $Na_2S_2O_3$ concentration corresponds to a gradual rise in the energy bandgap**.** Atomic force microscopy (AFM) revealed that root mean square (RMS) roughness consistently decreased with increasing annealing temperature. However, changes in sodium thiosulfate concentration did not produce a clear trend in surface morphology. The surface roughness varied across different concentrations. Scanning electron microscopy (SEM) images showed the formation of large, mushroom-shaped grains around 8 µm in size, which reduced with annealing. The strong light absorption in both visible and ultraviolet regions suggests that Sb_2S_3 is a promising material for solar cell absorber layers and photodetector applications**.**

Key words: Antimony sulphide, CBD, sodium thiosulphate, absorption, visible, ultraviolet

INTRODUCTION

The advancement of thin-film solar cell technology has gained significant momentum in recent years, largely driven by the high production costs and complex fabrication processes associated with traditional silicon-based photovoltaic devices. Materials such as cadmium telluride (CdTe) and copper indium gallium diselenide (CIGS) have emerged as leading absorber layers, while cadmium sulfide (CdS) continues to be widely used as a window layer in thin-film solar cells (Hafaifa et al., 2024; Zayas-Bazan et al, 2018). However, the limited availability of tellurium (Te) and indium (In), coupled with the environmental toxicity of cadmium (Cd), has necessitated the exploration of alternative

absorber and buffer materials that are both non-toxic and earth-abundant. In this context, antimony sulphide **(**Sb_2S_3**)** has garnered increasing attention for optoelectronic and photovoltaic applications due to its favourable bandgap (~1.77 eV)**,** high absorption coefficient**,** low environmental impact**,** and natural abundance (Alemi et al., 2011; Pareek et al., 2025; Alsulami, 2025; Gilshtein et al., 2025; Gomaa et al., 2023; Li et al., 2025). **Sb_2S_3** and Sb_2Se_3-based solar cells exhibit a comparatively lower environmental footprint than CdTe and perovskite photovoltaic technologies, primarily due to the abundance and low toxicity of their constituent elements**.** Although antimony extraction does present some environmental concerns, these are generally less severe than those associated with the sourcing of rarer or more hazardous elements used in CdTe and perovskite cells (Ezihe et al., 2025a).

With optimized material processing and resource management, Sb_2S_3/Sb_2Se_3 demonstrates strong potential as a sustainable absorber material. Its inherently low toxicity and the widespread availability of its key elements particularly when contrasted with the limited supply of materials such as tellurium, indium and toxicity of materials like cadmium, lead positions it as a promising candidate for scalable and environmentally sustainable solar energy deployment. By contrast, while CdTe cells benefit from established recycling infrastructure, their long-term sustainability is constrained by the scarcity of tellurium and the toxic nature of cadmium. Although recycling mitigates some of these risks, continued reliance on tellurium extraction presents ongoing challenges to the viability of CdTe-based systems (Ezihe et al., 2025b). Structurally, Sb_2S_3 possesses a distinctive one-dimensional crystal arrangement comprising covalently bonded $(Sb_4S_6)_n$ ribbons, held together by van der Waals forces (Zhou et al., 2022). This anisotropic structure results in direction-dependent optical and electronic properties, which can be exploited for improved charge transport. While much of the existing work on Sb_2**S_3**-based solar cells has focused on optimizing grain orientation in planar thin films, its inherent one-dimensionality makes nanorod architectures particularly promising for achieving efficient, directed carrier transport across device interfaces (Farhana et al., 2023). Heterojunction solar cells incorporating p-type Sb_2S_3 and n-type CdS have demonstrated power conversion efficiencies approaching 7% (Wang et al., 2018; Younsi et al., 2024). Furthermore, **S**b_2S_3 also serves as a viable precursor for the synthesis of other copper-antimony-sulfide absorber materials, including $CuSbS_2$, Cu_3SbS_3, Cu_3SbS_4, and $Cu_{12}Sb_{13}S_{16}$ (Chalapathi et al., 2020).

In this work, Sb_2S_3 thin films were synthesized via the chemical bath deposition (CBD) technique, which offers precise tunability of film thickness and composition through the adjustment of parameters such as solution pH, temperature, and precursor concentrations**.** CBD is particularly advantageous due to its cost-effectiveness and capability to achieve uniform coverage over large-area substrates. We explore the impact of varying sodium thiosulfate ($Na_2S_2O_3$) concentrations on the optical and morphological characteristics of Sb_2S_3 thin films, along with the influence of post-deposition annealing. The absorption behaviour did not exhibit a consistent trend with changes in precursor molarity; however, an increase in sodium thiosulfate concentration was associated with a gradual widening of the optical bandgap**.** X-ray diffraction (XRD) analysis revealed that annealing promoted the formation of a polycrystalline stibnite phase with an orthorhombic crystal structure, indicating improved crystallinity with thermal treatment.

2. Experimental Methods

Chemical bath deposition was used to synthesize the materials. This method has been reported by (Sharma et al., 2020; Parize et al., 2027). Owing to its low cost, simplicity, and suitability for large-area film fabrication, this method is favoured over vacuum-based deposition techniques**.** Before

deposition, the substrates were degreased by immersion in HCl for 3 hours, followed by cleaning with detergent, rinsing with distilled water, and air drying. This cleaning process enhances the surface by creating effective nucleation sites, which promotes uniform film growth and strong adhesion. The synthesis of Sb_2S_3 is facilitated using the following chemical precursors and complexing agents. The precursor solutions were made with analytical reagent (AR) grade chemicals. Antimony trichloride ($SbCl_3$) acts as the antimony (Sb) precursor, Sodium thiosulphate as a precursor for sulphur S, acetone as the complexing agent. Complexing agent controls the concentration of metal ions during thin film deposition, preventing rapid precipitation, promoting ion-by-ion growth, and stabilizing the deposition bath. By controlling the release of precursor ions, they enhance film properties such as adhesion, crystallinity, uniformity and thickness (Ezihe et al., 2019). 0.65g of $SbCl_3$ was dissolved in 2.5ml of acetone and stirred for 3 minutes, and then 1 M of sodium thiosulphate was added to the solution and stirred for 1 minute, and ionized water took the volume to 100 ml. The acidic environment necessary for the film growth was maintained at pH of 2.72. The film was grown on the glass substrate over a duration of 1 hour at a deposition temperature of 55 °C. This procedure was repeated using sodium thiosulfate concentrations of 1.5 M, 2.0 M, 2.5 M, and 3.0 M. The corresponding chemical reactions involved in the deposition process are outlined in Equations 1–4.

Sodium thiosulfate formed complex with antimony chloride

$$2SbCl_3 + 3Na_2S_2O_3 \rightarrow Sb_2(S_2O_3)_3 + 6NaCl \quad (1)$$

Dissociation of the antimony thiosulfate complex releases Sb^{3+} ion

$$Sb_2(S_2O_3)_3 \rightleftharpoons 2Sb^{3+} + 3S_2O_3^{2-} \quad (2)$$

And hydrolysis of thiosulfate releases sulphide ion

$$S_2O_3^{2-} + H_2O \rightleftharpoons SO_4^{2-} + S^{2-} + 2H^+ \quad (3)$$

The growth mechanism of Sb_2S_3 is ion-by-ion condensation, i.e. Sb^{3+} and S^{2-} ions condensing on the substrate to form Sb_2S_3

$$2Sb^{3+} + 3S^{2-} \rightleftharpoons Sb_2S_3(s) \quad (4)$$

The slides were taken out, rinsed with distilled water, and left to air dry. The freshly deposited thin films exhibited a orange colour and were stored in a slide box. Some of these samples were later annealed in air at 200 °C for 25 minutes before undergoing further analysis.

The Sb_2S_3 thin films were thoroughly analyzed to determine their structural, optical and surface characteristics. X-ray diffraction (XRD) analysis was performed using a Shimadzu XRD-6000 diffractometer with Cu-Kα radiation (λ = 1.5406 Å) to examine the crystal structure. Optical properties, such as absorbance and reflectance across the 200–1100 nm wavelength range, were measured using a PerkinElmer UV-Vis-NIR spectrophotometer.Atomic Force Microscopy (AFM) was employed with a Stromlingo DIY system to assess surface topography, while surface morphology was further studied using a 2023 model Axia ChemiSEM from Thermo Scientific.

3. Results and Discussions

The XRD plot of as-synthesized Sb_2S_3 shows no diffraction peaks, indicating amorphous state of the material. When annealed at 200 °C the film exhibited diffraction peaks at 2θ equals 34.0°, 37.9°, and 44.1° corresponding to planes (301), (231) and (250) respectively. These diffraction peaks has been reported in the literature by Oommen et al. and Ezema et al. (Oommen et al., 2010; Ezema et al., 2007). The observed peaks are in significant agreement with the powder diffraction and standards Ref file: PDF # 42-1393. X-ray diffraction analysis showed that annealing facilitated the formation of a polycrystalline stibnite phase with an orthorhombic crystal structure, suggesting enhanced crystallinity as a result of thermal treatment.

Table 1 gives the crystal structure parameters of as-synthesized and annealed Sb_2S_3. From the plots, as-synthesized sample displays no peaks showing that the material is amorphous. When annealed, the material displays peaks as can be seen from the XRD plots. It could be seen from the plots that the plane with the highest intensity is (231) plane which of course is the preferential plane for the crystallites of the films. The crystallite size of the preferential orientation is 44 nm, the full width at half maximum is 0.2 ° and the inter-planer spacing is about 2.37 Å.

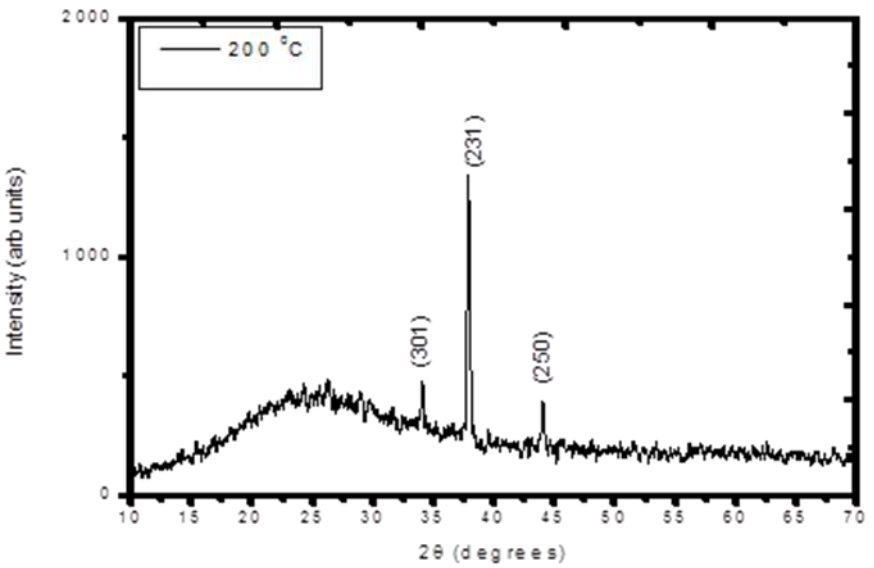

Figure 1: (a) XRD spectrum of 200 °C annealed Sb_2S_3 thin film

Sb_2S_3 amorphous materials lack a regular atomic structure, i.e. they are noncrystalline. When used in solar cell it exhibits lower conversion efficiency under optimal conditions but may have a higher light absorption rate than the crystalline phase. They exhibit a superior performance in low-light and shaded conditions and are ideal for flexible solar applications, such as small devices and building

integrated photovoltaics (BIPV) where flexibility is a key advantage (Smith et al., 2024; Hossen et al., 2022). Crystalline Sb_2S_3 solar cells, by contrast, possess a highly ordered atomic lattice, often derived from single crystals or polycrystalline grains**.** They generally offer higher efficiency under direct sunlight but are less tolerant to partial shading, as shadowing disrupts the uniform charge transport enabled by the ordered structure, the specific 1D ribbon structure of Sb_2S_3 and its control over carrier transport are key factors in its efficiency and shading sensitivity (Farhana et al., 2023). Crystalline technologies are typically employed in conventional solar installations where maximum efficiency and long-term durability are critical.

Table 1: Crystal structure parameters of as-synthesized and annealed Sb_2S_3

As-deposited				**Annealed (200 ^{0}C)**				
2θ (°)	**(hkl)**	***d*-spacing (Å)**	**β (°)**	***D* (nm)**	**2θ (°)**	**(hkl)**	***d*-spacing (Å)**	**β (°)**	***D* (nm)**
`					34.0	(301)	2.63	0.4	22
Amorphous					37.9	(231)	2.37	0.2	44
					44.0	(250)	2.06	0.3	30

Graph of optical absorbance against wavelength for various molar concentrations of sulphur precursor i.e. sodium thiosulphite ($Na_2S_2O_3$) of un-annealed Sb_2S_3 thin film materials is shown in Figure 2a, for wavelength range of 200nm to 1000nm. With increased concentration of sulphur, the absorption edge exhibited a great shift in the UV region for as grown films. The highest absorption occurred at UV region (323 nm) for 2.5 M film with a value of 99%. That of 2.0 M film rose from the UV into the visible around the blue line (994 nm) with absorbance of 99% which is the highest in the visible; it fell steadily down to the infrared region of the spectrum for the un-annealed materials. The sample with the lowest absorbance across the solar spectrum was the 3.0 M film with 0.19% in UV, 0.13% in the visible and 0.02% in the NIR. For annealed material Figure 2b, similar scenario played out but this time with 1 M and 2.5 M grown film having the best absorbance in the UV and 2.0 M having the best absorbance in the visible region. The highest absorption took place at UV region with a value of 99 % at 343 nm wavelength for 1 M and 2.5 M films. Again, at the blue line (450-495 nm) the absorbance of 2.0 M sample rose to 99 % and thereafter decreased steeply to near infrared region of the spectrum. Again, the film with the lowest absorbance across the solar spectrum is the 3.0 M grown film with the lowest value at the near infrared region of the spectrum. The variation of the molarity of the surphur precursor did not uniformly influence the absorbance of the materials. Variation of these concentrations may create defects such as antimony vacancies; alter the microstructure, optical properties, electrical properties and overall properties of the material. High absorption for 2.0 M Sb_2S_3 film in the visible underscores that it is the ideal concentration for solar cell application, and that of 2.5 M film can be used in UV shielding because of its high absorption in the UV region of the spectrum.

Figure 2c presents graph of optical reflectance against wavelength for various molar concentrations of sulphur precursor ($Na_2S_2O_3$) of un-annealed Sb_2S_3 thin film material. We observed that 3.0 M sample with the least absorbance has the highest reflectance. This is in order because the amount of light reflected will definitely reduce the amount that will be absorbed. For the annealed materials, Figure 2d, the trend is similar with the as-synthesized materials. Generally, annealed materials have higher reflectance compared to as-deposited materials. For the purpose of absorption layer in solar cell application 2.0 M is the optimized molarity.

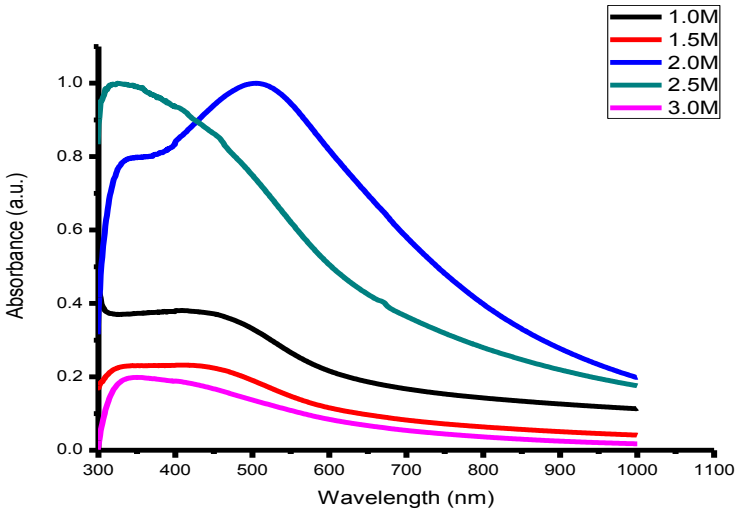

Figure 2a: Graph of optical absorbance against wavelength for various molar concentrations of sulphur precursor ($Na_2S_2O_3$) of as-deposited Sb_2S_3 thin film material.

The plot of direct energy bandgap against photon energy for various concentrations of sulphur precursor ($Na_2S_2O_3$) of as-deposited Sb_2S_3 thin film material is given in Figure 2e. Determination of direct band gap energy by the plot of square of absorbance vs photon energy has been reported by some authors in the literature (Ojo & Dharmadasa, 2017; Echendu et al., 2018; Olusola et al., 2017). From the graph the direct band energy of 1.0 M grown film was estimated 1.30 eV, 1.5 M was 1.95 eV, 2.0 M was 1.49 eV, 2.5 M was 1.77 eV and 3.0 M was 1.93 eV, which showed relative increase with the molarity of the sulphur precursor. The direct energy bandgap values are in agreement with reported values for these films in lieratures (Avilez Garcia et al., 2016; Chalapathi et al., 2020). Figure 2f presents plot of energy bandgap against photon energy for various concentrations of sulphur precursor ($Na_2S_2O_3$) of annealed Sb_2S_3 thin film material. The bandgap estimation from the plot for 1.0 M film was 1.56 eV which is higher compared to the as-deposited film 1.30 eV. The same trend was exhibited by 1.5 M grown film with 2.30 eV which is higher than that of as-deposited 1.95 eV, but 2.0 M film with 1.34 eV is lower than 1.49 eV of as-deposited and 2.5 M film with 1.92 eV higher

than 1.77 eV of as-deposited, also, 3.0 M annealed film with band energy of 2.07 eV is little higher than the as-deposited film with 1.93 eV. The increased in band energy could be attributed to quantum confinement effect due to decrease in particle size (Krishnan et al., 2008). The energy bandgap relatively increases with increase in molar concentration of sodium thiosulphate. We precisely controlled the constituent concentrations of the precursors to achieve a single phase thin film which is crucial for cell optimal performance. The bandgap energy is in tandem with our proposed Sb_2S_3/Sb_2Se_3 absorber layer for thin film solar cell application.

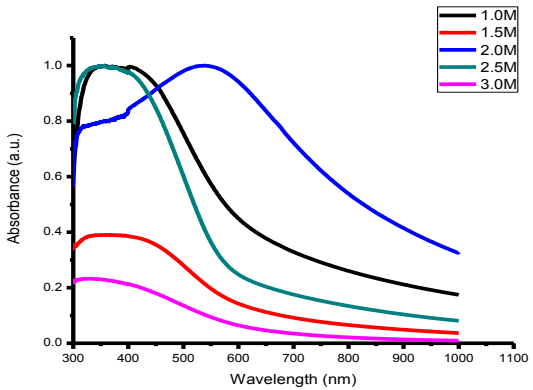

Figure 2b: Graph of optical absorbance against wavelength for various molar concentrations of sulphur precursor ($Na_2S_2O_3$) 198 °C annealed Sb_2S_3 thin film material.

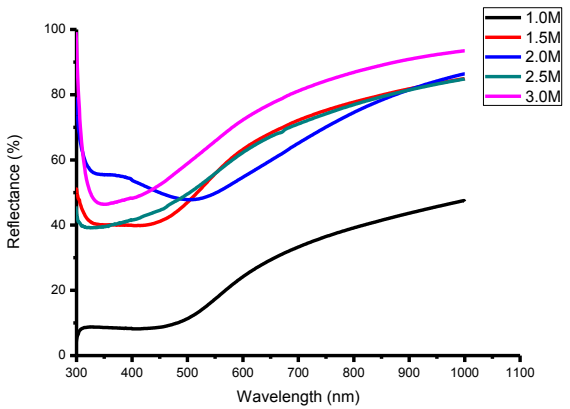

Figure 2c: Graph of optical reflectance against wavelength for various molar concentrations of sulphur precursor ($Na_2S_2O_3$) of as-synthsized Sb_2S_3 thin film material.

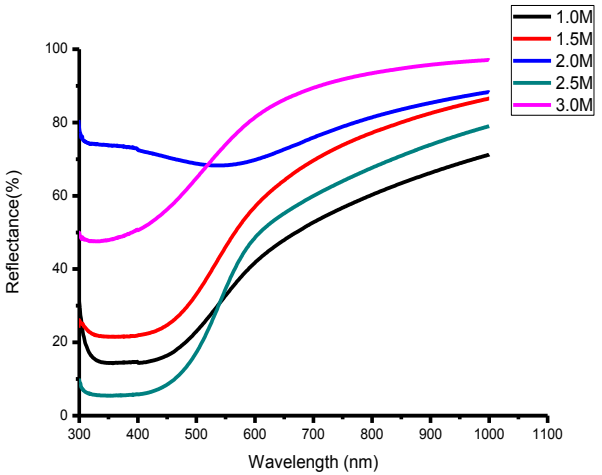

Figure 2d: Graph of optical reflectance against wavelength for various molar concentrations of sulphur precursor ($Na_2S_2O_3$) 198 °C annealed Sb_2S_3 thin film material

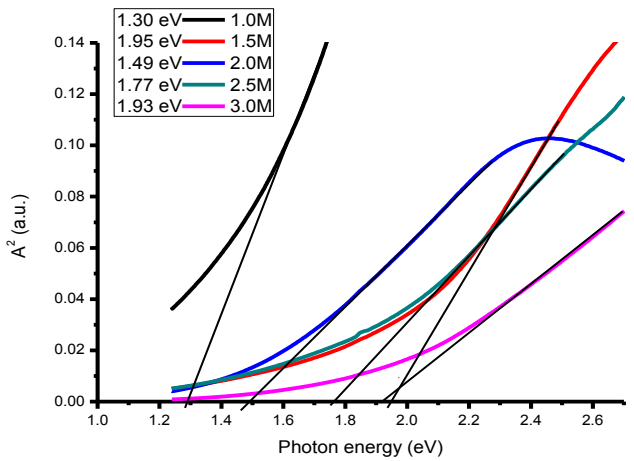

Figure 2e: Plot of energy bandgap against photon energy for various concentrations of sulphur precursor ($Na_2S_2O_3$) of as-deposited Sb_2S_3 thin film material.

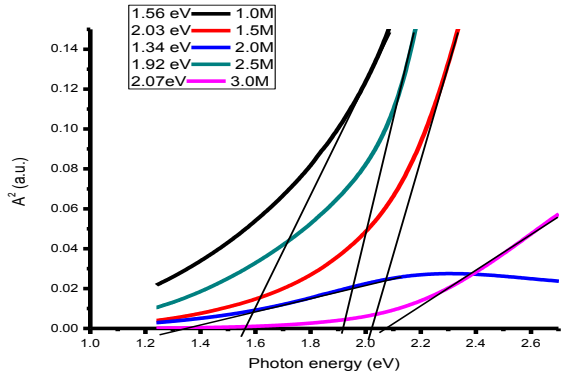

Figure 2f: Plot of energy bandgap against photon energy for various concentrations of sulphur precursor ($Na_2S_2O_3$) 198 °C annealed Sb_2S_3 thin film material.

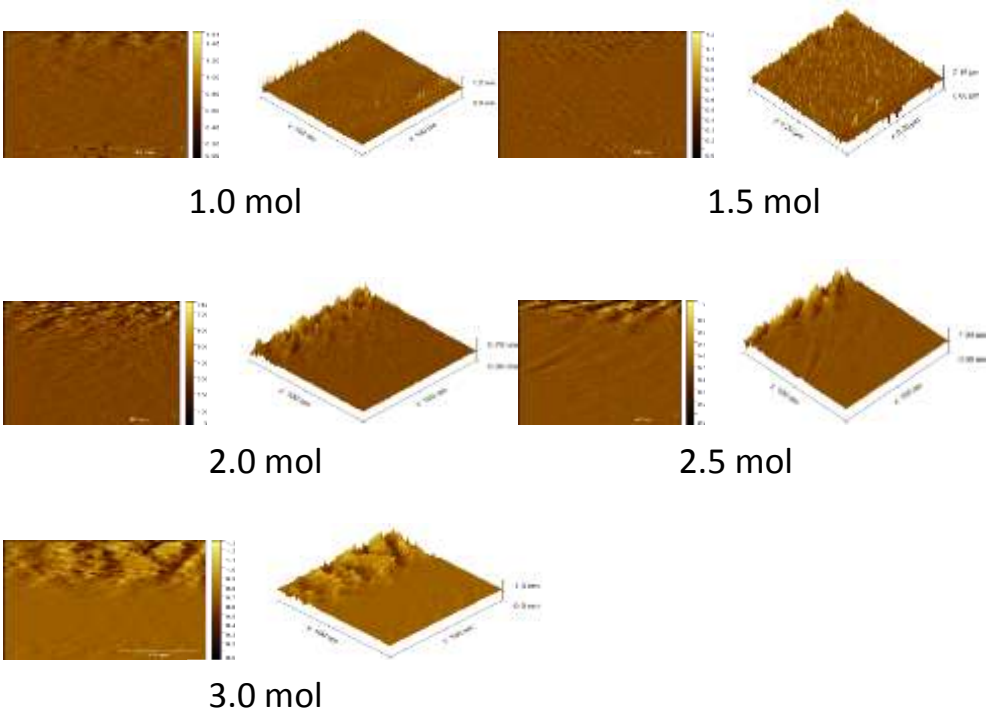

Figure 3a: AFM images for 2 and 3 – dimensions of various molar concentrations of sulphur precursor ($Na_2S_2O_3$) of as-deposited Sb_2S_3 thin film material

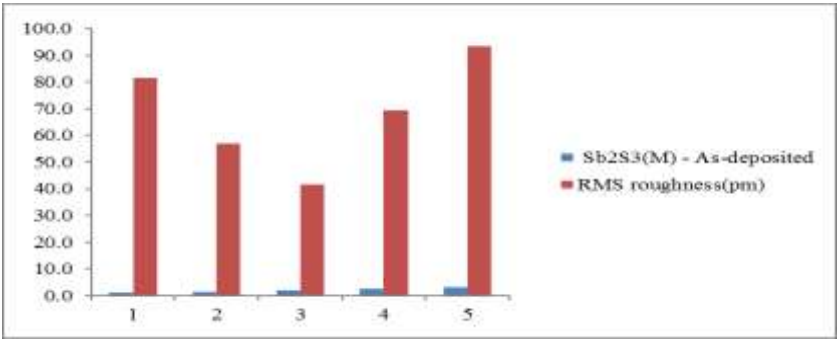

Figure 3b: Bar chart of RMS roughness of AFM images of various molar concentrations of sulphur precursor ($Na_2S_2O_3$) of as-deposited Sb_2S_3 thin film material

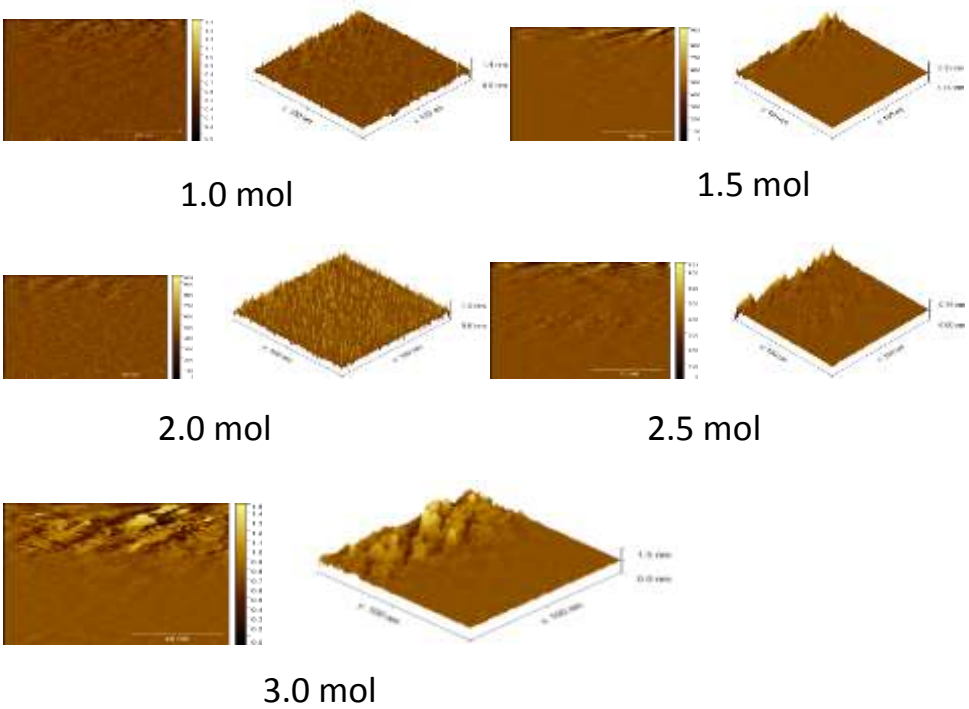

Figure 3c: AFM images for 2 and 3 – dimensions of various molar concentrations of sulphur precursor ($Na_2S_2O_3$) of annealed Sb_2S_3 thin film material.

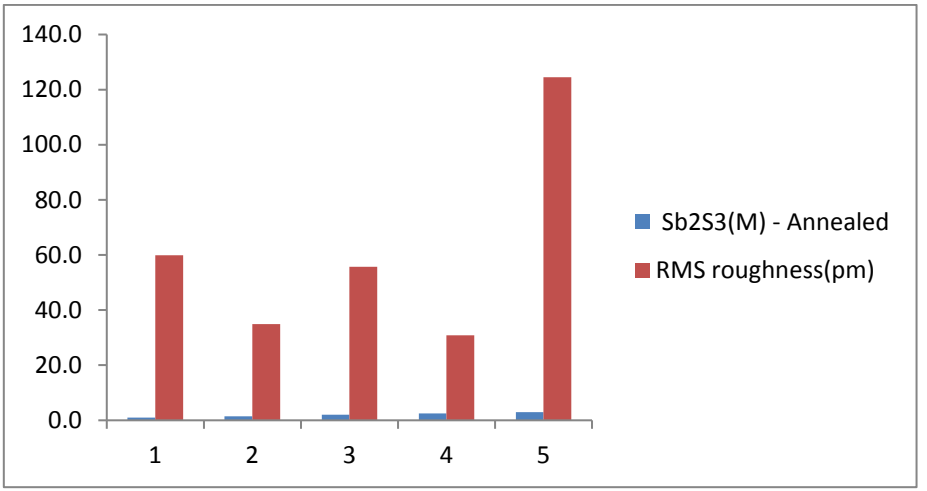

Figure 3d: Bar chart of RMS roughness of AFM images of various molar concentrations of sulphur precursor ($Na_2S_2O_3$) of annealed Sb_2S_3 thin film material.

SEM images of different magnifications of (a.) as-deposited and (b.) annealed Sb_2S_3 thin film materials are presented in figure 4a. From the 10000 magnification of as-deposited film Figure 4a, a giant mush room grain of estimated size of 8 µm is observed around the center of the sample. Also noticed are isolated grains of various sizes and shapes with estimated grain sizes ranging from 5µm to 1.5µm. Agglomeration of surface particles has been consistently identified as a prevalent morphological feature in Sb_2S_3 thin films synthesized using this method, as documented in several studies (Lokhandea et al., 2002; Salem & Selim, 2001). This characteristic is often attributed to the nature of the deposition process, which promotes particle clustering during film growth. There is a single cluster at the center of the annealed film material Figure 4b with estimated length of 6µm and width of 2µm. We also observed interlocking grains of regular patterns of estimated sizes of 0.2µm. The large mushroom shaped grain shows more compact films with fewer grain boundaries - which serves as trap centers for charge carriers. This large grain minimizes recombination losses, reduces defects, enhances carrier mobility and improves open-circuit voltage (V_{oc}), short circuit current (I_{sh}) leading to higher cell efficiency.

Although Sb_2S_3 thin-film solar cells currently demonstrate lower power conversion efficiencies compared to established technologies such as CdTe and CIGS (Gu, et al., 2024a), they offer several compelling advantages for next-generation photovoltaic applications. A major benefit is their reduced environmental footprint, as Sb_2S_3 does not incorporate toxic or scarce elements, making it a more sustainable alternative. Furthermore, the constituent materials are abundant and potentially more economical, enhancing their viability for large-scale deployment. Sb_2S_3-based devices also exhibit excellent thermal and chemical stability, which is critical for ensuring long-term operational reliability and performance retention. When Sb_2S_3 is combined with Sb_2Se_3 in a dual absorber configuration, the absorption spectrum is effectively extended into the near-infrared (NIR) region.

a.

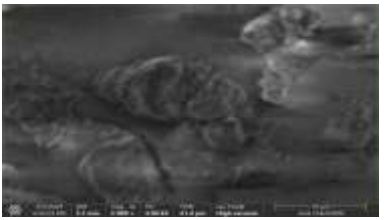

5000X

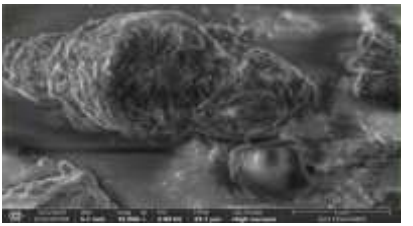

10000X

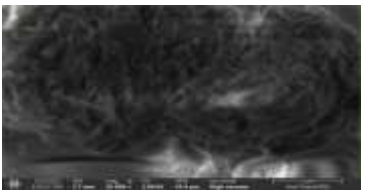

20000X

b.

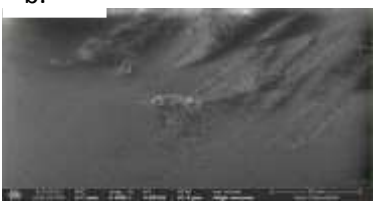

5000X

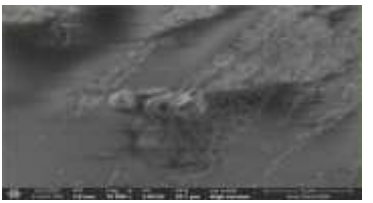

10000X

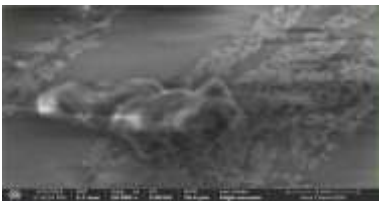

20000X

Figure 4a: SEM images of different magnifications of (a.) as-deposited and (b.) annealed Sb_2S_3 thin film materials

This enhancement arises from the narrower bandgap of Sb_2Se_3 (~1.1 eV)**,** which enables it to absorb photons in the infrared portion of the solar spectrum complementing the visible light absorption provided by Sb_2S_3 (Gu, et al., 2024b; Deng et al., 2022)**.** As a result, the integrated Sb_2S_3/Sb_2Se_3 system offers broader spectral coverage**,** improving the potential for enhanced photogeneration and solar energy conversion efficiency across a wider range of wavelengths, including the NIR region**.**

5. Conclusion

In this work, Sb2S3 thin films were synthesized as part of dual absorber architecture in combination with Sb2Se3, employing a cost-effective and reproducible chemical bath deposition (CBD) method for potential application in photovoltaic devices. The study focused on evaluating the effect of varying sodium thiosulfate ($Na_2S_2O_3$) concentrations on the optical and morphological properties of Sb_2S_3 films, along with the influence of post-deposition annealing**.** X-ray diffraction (XRD) analysis confirmed that the as-deposited Sb_2S_3 films were amorphous**,** with a notable improvement in crystallinity observed after annealing at 200 °C. Optical characterization indicated that films prepared with 2.0 M and 2.5 M thiosulphate concentrations provided optimal absorption in the visible and ultraviolet spectral regions, respectively. The films also exhibited a direct optical bandgap, which increased progressively with rising precursor concentration. An optimal bandgap value of ~1.77 eV was obtained, aligning well with the requirements for efficient solar energy conversion in Sb_2S_3/Sb_2Se_3 tandem absorber solar cells**.** Atomic force microscopy (AFM) revealed no consistent trend in microstructural morphology as a function of sodium thiosulfate concentration. However, surface roughness exhibited non-uniform variation with molarity. Scanning electron microscopy (SEM) images showed the presence of large, mushroom-like grains (~8 μm) in the as-synthesized films, which were significantly reduced in size following thermal treatment. The high optical absorption in both the UV and visible regions, along with the tunable bandgap and improved crystallinity post-annealing, demonstrates the promise of Sb_2S_3 as an effective material for photodetector applications and as an absorber layer in thin-film solar cell devices**,** particularly in Sb_2S_3/Sb_2Se_3 heterostructures.

Conflict of Interest: The author declared that there is no conflict of interest.

REFERENCES

Alemi, A., Hanifehpour, Y. & Joo, S. (2011). Synthesis and Characterization of Sb_2S_3 Nanorods via Complex Decomposition Approach. *Journal of Nanomaterials*, 10.1155/2011/414798

Alsulami, A. (2025). Synthesis and characterization of the Al: Sb_2S_3 thin films: Impact of Aluminum doping on the structural, optical, and optoelectrical properties. *Indian Journal of Physics*, 10.1007/s12648-025-03767-x.

Avilez Garcia, R. G., Meza Avendaño, C. A., Mou, P., Delgado, F. P., & Mathews, N. R. (2016). Antimonysulfide (Sb_2S_3) thin films bypulseelectrodeposition: Effect of thermal treatment on structural, optical and electrical properties. *Materials Science in Semiconductor Processing*, 4491–100, http://dx.doi.org/10.1016/j.mssp.2015.12.018

Chalapathi, U., Poornaprakash, B., & Park, S. H. (2020). Influence of post-deposition annealing temperature on the growth of chemically deposited Sb_2S_3 thin films. *Superlattices and Microstructures*, 141106500, https://doi.org/10.1016/j.spmi.2020.106500

Deng, H., Chen, S., Ishaq, M., Cheng, Y., Sun,Lin, Q. X., …& Cheng, S. (2022). Efficient All-Inorganic Sb_2S_3 Solar Cells with Matched Energy Levels Using Sb_2Se_3 as Hole Transport Layers. *Solar RRL*. 6. 10.1002/solr.202101017.

Echendu, O. K., Werta, S. Z., & Dejene, F. B. (2018). Effect of cadmium precursor on the physico-chemical properties of electrochemically grown CdS thin films for optoelectroniccs devices application: a comparative study. *Journal of Material Science: Materials in Electronics*, 30 (365-377)

Ezema, F. I., Ekwealor, A. B., Asogwa, P. U., Ugwuoke, P. E., Chigbo C., & Osuji, R. U. (2007). Optical Properties and Structural Characterizations of Sb_2S_3 Thin Films Deposited by Chemical Bath Deposition Technique. *Turkish Journal of Physics*: 31(4) 4, https://journals.tubitak.gov.tr/physics/vol31/iss4/4

Ezihe, J., Eya, D. D. O., Iroegbu, C., Echendu, O. K., & Egbo, K. O. (2019). Characterization of Nanocrystallite $CdAl_2SO_3$ Thin Films Produced by Inexpensive Chemical Bath Techniques for Photonic Device Applications: The Influence of Annealing Temperature,'' *To Physics Journal*, 3(2581-7396), http://www.purkh.com/index.php/tophy

Ezihe, J. A., Abdulwahab, M., Ezema, F. I., & Echendu, O. K. (2025a). Development of chalcogenide Sb_2Se_3 thin film by simple and low-cost chemical bath deposition technique for optoelectronics applications. *Journal of Nano and Materials Science Research*, 3(2), 21–27, https://doi.org.10.20221/jnmsr.v3i2.35

Ezihe, J. A., Abdulwahab, M., Ezema, F. I. & Echendu, O. K. (2025b). Essential properties, growth methods, environmental impacts, and solar cell application of antimony triselenide thin films: A review. *Hybrid Advances*, 10 (100505), https://doi.org.10.1016/j.hybadv.2025.100505.

Farhana, M., Manjceevan, A., & Bandara, J. (2023). Recent advances and new research trends in Sb_2S_3 thin film based solar cells. *Journal of Science: Advanced Materials and Devices*, 8 (100533), 10.1016/j.jsamd.2023.100533.

Gilshtein, E., Gupta, H. M., Enevoldsen, A. M. P., Besleaga, C., Galca, A. C., & Canulescu, S. (2025). Superstrate structured Sb_2S_3 thin-film solar cells by magnetron sputtering of Sb and

post-sulfurization. *Materials & Design*, 258 (114621), https://doi.org/10.1016/j.matdes.2025.114621.

Gomaa, M. M., Sayed, M. H., Abdel-Wahed, M. S., & Boshta, M. (2023). Synthesis of Sb_2S_3 nanosphere layer by chemical bath deposition for the photocatalytic degradation of methylene blue dye. *RSC Adv.*, 21,3(32), 22054-22060, doi: 10.1039/d3ra02062b. PMID: 37483670; PMCID: PMC10359849.

Gu, S., Ullah, S., Khan, F., Wang, X., Liu, P., Yang S., & Y. Chen (2024a). Recent advances and perspectives on Sb_2S_3 thin-film solar cells. *Materials Today Sustainability*, 28 (101019), https://doi.org/10.1016/j.mtsust.2024.101019

Gu, S., Ullah, S., Wang, X., Liu, P., Yang, S. & Chen, Y. (2024b). Recent advances and perspectives on Sb_2S_3 thin-film solar cells. *Materials Today Sustainability*, 28. 101019. 10.1016/j.mtsust.2024.101019.

Hafaifa, L., Maache, M., & Bouabdelli, M. W. (2024). Improved performance of CdTe thin-film solar cell through key parameters. *Journal of Theoretical and Applied Physics (JTAP)*, 18 (3)182435, 1-10 https://dx.doi.org/10.57647/j.jtap.2024.1803.35

Hossen, M. S., Alam, K., Mostakim, M., Mahmud, U., Imran, M. A., & Fathah, A. A. (2022). Integrating Solar Cells into Building Materials (Building-Integrated Photovoltaics - BIPV) to Turn Buildings into Self-Sustaining Energy Sources. *International Journal of Scientific Research and Management (IJSRM)*, 10 (946-962), 10.18535/ijsrm/v10i9.ec05.

Krishnan, B., Arato, A., Cardenas, E., Das Roy, T. K., & Castillo, G. A., (2008). On the structure, morphology, and optical properties of chemical bath deposited Sb_2S_3 thin films. *Applied Surface Science*, 25 (3200–3206), doi:10.1016/j.apsusc.2007.10.098

Li, X., Yang, Y., Feng, L., Yang, Y., Hu, K., …& Zhang, Y. (2025). Tailoring Presynthesized Amorphous Sb_2S_3 Particles Enables High-Efficiency Pure Antimony Sulfide Solar Cells. *ACS Applied Materials & Interfaces*, 17 (11), 16738-16746, DOI: 10.1021/acsami.4c17684

Lokhandea, C. D., Sankapala, B. R., Mane, R. S., Pathan, H. M., Muller, M., & Ganeshan, V. (2002). Structural characterization of chemically deposited Bi_2S_3 thin Bi_2Se_3 thin films. *Applied Surface Science*, 187 (1–2), 108–115, https://doi.org/doi.org/10.1016/S0169-4332(01)00813-3

Ojo, A. A., & Dharmadasa, I. M. (2017). Analysis of the electronic properties of all-electroplated ZnS, CdS and CdTe graded bandgap photovoltaic device configuration. *Solar Energy*, 158 (721–727), http://dx.doi.org/10.1016/j.solener.2017.10.042

Olusola, O. I., Madugu, M. L., & Dharmadasa, I. M. (2017). Investigating the electronic properties of multi-junction ZnS/CdS/CdTe graded bandgap solar cells. *Materials Chemistry and Physics*, S0254-0584, 30053-6, doi:10.1016/j.matchemphys.2017.01.027

Oommen, R., Jessy M. N., & Usha, R. P. (2010). Structural and Morphological Studies of Sb_2S_3 Thin Films. *Journal of Ovonic Research*, 6 (6), 259-266.

Pareek, A., Katerski, A., Kriisa, M. et al. (2025). Towards all inorganic antimony sulphide semitransparent solar cells. *Sci Rep*, 15 (1468), https://doi.org/10.1038/s41598-025-85676-x

Parize, R., Cossuet, T., Chaix-Pluchery, O., Roussel, H., Appert, E., & Consonni, V. (2017). In situ analysis of the crystallization process of Sb2S3 thin films by Raman scattering and X-raydiffraction. *Jmade*, doi: 10.1016/j.matdes.2017.02.034

Salem, A. M., & Selim, M. S. (2001). Structure and optical properties of chemically deposited Sb_2S_3 thin films,'' *J. Phys. D Appl. Phys.*, 34 (12), DOI 10.1088/0022-3727/34/1/303.

Sharma, V., Das, T. K., & Ilaiyaraja, P. (2020). Growth of Sb_2S_3 Semiconductor Thin Film on Different Morphologies of TiO_2 Nanostructures. *Materials Research Bulletin*, doi: https://doi.org/10.1016/j.materresbull.2020.110980

Smith, A.R., Ghamari, M., Velusamy, S., & Sundaram, S. (2024). Thin-Film Technologies for Sustainable Building-Integrated Photovoltaics. *Energies*, 17, 6363, https://doi.org/10.3390/en17246363

Wang, K., Cheng, J., Yang, X., et al. (2018). Enhanced Photovoltaic Properties in Sb_2S_3 Planar Heterojunction Solar Cell with a Fast Selenylation Approach. *Nanoscale Res Lett*, 13, (270), https://doi.org/10.1186/s11671-018-2651-x

Younsi, Z., Meddour, F., Bencherif, H., et al. (2024). Scrutinizing transport phenomena and recombination mechanisms in thin film Sb_2S_3 solar cells. *Sci Rep*, 14 (12460), https://doi.org/10.1038/s41598-024-56041-1

Zayas-Bazan, P. G., Zayas-Bazan, K. G. & deMelo., O. A. J. (2018). Study of CdS nanowires for use as window material in CdS/CdTe solar cells. *IEEE 7th World Conference on Photovoltaic Energy Ceonversieon*. https://doi.org/10.11109/PVSC.2018.8547308

Zhou, B., Hayashi, T., Hachiya K., & Sagawa, T. (2022). Preparation of Sb2S3 nanorod arrays by hydrothermal method as light absorbing layer for Sb2S3-based solar cells. *Thin Solid Films*. 757, (139389), 2022 10.1016/j.tsf.2022.139389.